Dynamics of laser-driven heavy-ion acceleration clarified by ion charge states

M. Nishiuchi,[1,2] N. P. Dover,[1] M. Hata,[3] H. Sakaki,[1] Ko. Kondo,[1] H. F. Lowe,[1] T. Miyahara,[1,7] H. Kiriyama,[1] J. K. Koga,[1] N. Iwata,[3] M. A. Alkhimova,[4,5] A. S. Pirozhkov,[1] A. Ya. Faenov,[6,5] T. A. Pikuz,[6,5] A. Sagisaka,[1] Y. Watanabe,[7] M. Kando,[1] K. Kondo,[1] E. J. Ditter,[8] O. C. Ettlinger,[8] G. S. Hicks,[8] Z. Najmudin,[8] T. Ziegler,[9] K. Zeil,[9] U. Schramm,[9] and Y. Sentoku[3]

[1]*Kansai Photon Science Institute (KPSI), National Institutes for Quantum and Radiological Science and Technology (QST), 8-1-7 Umemidai, Kizugawa, Kyoto 619-0215, Japan*

[2]*PRESTO, Japan Science and Technology Agency, 4-1-8 Honcho, Kawaguchi, Saitama 332-0012, Japan*

[3]*Institute of Laser Engineering, Osaka University, 2-6 Yamadaoka, Suita, Osaka 565-0871, Japan*

[4]*National Research Nuclear University (MEPhI), Moscow 125412, Russia*

[5]*Joint Institute for High Temperatures, Russian Academy of Sciences, Moscow 125412, Russia*

[6]*Institute for Open and Transdisciplinary Research Initiative, Osaka University, Suita, Osaka 565-0871, Japan*

[7]*Interdisciplinary Graduate School of Engineering Sciences, Kyushu University, Kasuga, Fukuoka 816-8580, Japan*

[8]*John Adams Institute for Accelerator Science, Blackett Laboratory, Imperial College London, London SW7 2AZ, United Kingdom*

[9]*Helmholtz-Zentrum Dresden-Rossendorf, Bautzner Landstraße 400, 01328 Dresden, Germany*

(Received 25 December 2019; revised 28 March 2020; accepted 4 June 2020; published 15 July 2020)

Motivated by the development of next-generation heavy-ion sources, we have investigated the ionization and acceleration dynamics of an ultraintense laser-driven high-Z silver target, experimentally, numerically, and analytically. Using a novel ion measurement technique allowing us to uniquely identify silver ions, we experimentally demonstrate generation of highly charged silver ions ($Z^* = 45^{+2}_{-2}$) with energies of >20 MeV/nucleon (>2.2 GeV) from submicron silver targets driven by a laser with intensity 5×10^{21} W/cm^2, with increasing ion energy and charge state for decreasing target thickness. We show that although target pre-expansion by the unavoidable rising edge of state-of-the-art high-power lasers can limit proton energies, it is advantageous for heavy-ion acceleration. Two-dimensional particle-in-cell simulations show that the Joule heating in the target bulk results in a high temperature (∼10 keV) solid density plasma, leading to the generation of high flux highly charged ions ($Z^* = 40^{+2}_{-2}$, $\gtrsim$10 MeV/nucleon) via electron collisional ionization, which are extracted and accelerated with a small divergence by an extreme sheath field at the target rear. However, with reduced target thickness this favorable acceleration is degraded due to the target deformation via laser hole boring, which accompanies higher energy ions with higher charge states but in an uncontrollable manner. Our elucidation of the fundamental processes of high-intensity laser-driven ionization and ion acceleration provides a path for improving the control and parameters of laser-driven heavy-ion sources, a key component for next-generation heavy-ion accelerators.

DOI: 10.1103/PhysRevResearch.2.033081

I. INTRODUCTION

Understanding and controlling a highly charged, high-density, and high-temperature extreme plasma produced by high-intensity short laser pulses interacting with solid targets can provide novel insights into high-energy physics, nuclear physics, and others [1]. These plasmas also provide a platform for transforming electromagnetic laser fields into quasielectrostatic fields, which can be used to accelerate particles. Neglecting relativistic effects, laser light propagates in a plasma up to the critical density n_{cr}, where the plasma frequency $\omega_p \equiv (4\pi e^2 n_e/m_e)^{1/2}$ (e, n_e, m_e, are electron charge, density, and mass, respectively) equals the laser frequency ω_L. The laser is then strongly absorbed, producing copious energetic electrons, which in turn produce extremely strong space-charge fields at the target surface, called the sheath. This allows ultrahigh gradient acceleration of high peak brightness beams of energetic ions, resulting in a compact ion source with a number of appealing uses [2–8].

In particular, there has been a lot of recent interest in the acceleration of high atomic number (high-Z) ions. Although conventional sources of low-Z ions are already relatively compact, high-Z sources cannot achieve high energies and charge states, resulting in heavy-ion accelerator complexes being extremely large with unavoidable beam emittance growth. Laser-accelerated heavy ions can provide, in a compact space both high charge states and moderately high energies ($\gtrsim$10 MeV/nucleon) with good emittance, making them an attractive replacement for the drift tube linacs typically used as the front end of conventional heavy-ion accelerator systems [9]. For example, a laser-driven alternative to conventional rare isotope beam (RIB) facilities has been proposed [7,8].

Several mechanisms of ultrahigh-intensity laser-driven ion acceleration from solid targets have been identified, including target normal sheath acceleration (TNSA) [10–12], radiation pressure acceleration [5,13–16], and the relativistically transparent or breakout after burner regimes [17,18], but most of these studies have focused on low-Z ion generation at intensities $<10^{21}$ W/cm^2, with maximum energies observed up to 48 MeV/nucleon and 80 MeV/nucleon for 10 J class [19] and 100 J class laser systems [20], respectively. For high-Z ions, the generation of highly charged low energy ($\leqslant$10 MeV/nucleon) beams has been demonstrated using lasers with intensities $<10^{21}$ W/cm^2 [21–24]. The acceleration of highly charged Fe ions up to energies of $\sim$15 MeV/nucleon has been demonstrated at intensities $\sim 10^{21}$ W/cm^2, but without direct discrimination of the ionization state [7,8]. To realize applications, even higher Z, and higher energy beams are required. Unfortunately, the ionization dynamics and the interplay with the acceleration mechanisms are far from being fully understood, as the laser-irradiated target is a highly nonequilibrium, dense and high-energy density plasma in an unexplored parameter regime. Furthermore, target surface contaminants effectively shield the target ions, preventing efficient acceleration without special treatment.

In this article we present an experimental, analytical and numerical investigation of the ionization and acceleration dynamics of highly charged silver ions from foils driven by a femtosecond PW-class laser pulse focused to a peak intensity of 5×10^{21} W/cm^2. By varying the silver foil thickness from 50 to 800 nm, we demonstrate the suppression of the maximum proton energy with thinner targets while simultaneously increasing the charge state and the maximum energies of the silver ions, unambiguously detected using a novel detector configuration. With an optimum target thickness of 500 nm, high flux highly charged (40^{+2}_{-2}) $\gtrsim$10 MeV/nucleon energy ions are observed, while for the thinnest target of 50 nm, maximum charge state and energy increased up to 45^{+2}_{-2} and 26^{+5}_{-4} MeV/nucleon, but the flux is reduced and the acceleration is less controllable. Combining analytical considerations with numerical hydrodynamic and particle-in-cell (PIC) simulations we show that the surface contaminant at the rear surface is preaccelerated and effectively blown off during the intrinsic relativistic rising edge in PW-class laser pulses, resulting in reduced contaminant ion energies but enhanced acceleration of bulk target ions. The bulk electron temperature in the target reached $\sim$10 keV, resulting in significant ionization of the silver M-shell and L-shell by collisions. These highly charged silver ions could subsequently be extracted by strong sheath fields of $\sim$40 to 80 TV/m at the target rear, without being shielded by surface contaminants.

Simulations show that the increase in charge state from the thinnest targets is due to additional field ionization by the intense field of the laser as it bores through the target. Therefore, by careful observation of the ion charge state, we have been able to investigate the transition between collisional and field ionized heavy-ion acceleration. Our investigation of the ionization and acceleration mechanisms of highly charged ions therefore provides a path for improving the control and capabilities of laser-driven heavy-ion sources, a key component for next-generation heavy-ion accelerators.

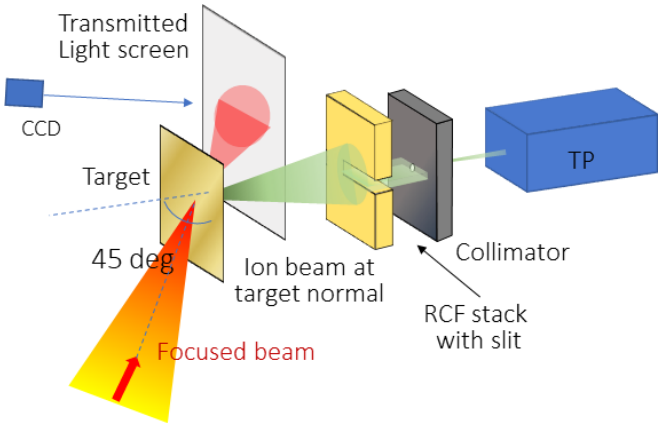

FIG. 1. Schematic view of the experimental setup.

II. EXPERIMENTAL RESULTS

The J-KAREN-P laser [25,26] [(12 ± 1) J, (40 ± 0.5) femtosecond (fs) FWHM, 800 nm wavelength, linear polarization] was focused using an f/1.4 off-axis parabola (OAP) to a spot size of (1.50 ± 0.05) μm diameter (FWHM), resulting in a peak intensity of 5×10^{21} W/cm^2 (cycle averaged) (Fig. 1), corresponding to a normalized vector potential $a_0 = eE_L/(m_e c\omega_L) = 50$ where e is the elementary charge, E_L the laser electric field amplitude, and c the speed of light. The temporal laser pulse shape was optimized by an acousto-optic programmable dispersive filter (AOPDF, by FastLite [27]). Silver target foils of thicknesses from 50 to 800 nm were placed at focus, at 45 degrees to the laser resulting in p-polarization. The laser contrast was measured just before the final focusing optic using a pick-off [Figs. 2(a) and 2(b)].

Radiochromic film (RCF) stacks [28] measured the proton beam profile on a single shot basis along the target normal direction, 50 mm behind the target. A slit in the center of the RCF stacks allowed coexistence with a Thomson parabola (TP) for concurrent quantification of the ion spectra in the target normal direction. The TP employed a 0.42 T magnetic field over 5 cm combined with an electric field of 30 kV/cm over 20 cm. The TP pinhole was set 430 mm away from the focus position with a solid angle of 265 nano-steradians. To allow conclusive identification of silver ions, we chose this solid angle such that ions appear as single-event ion tracks on the imaging plate (IP) detector, as shown in Fig. 3(a). In a TP, ions having the same charge to mass ratio fall onto the same parabolic trace on the detector. However, the photo-stimulated luminescence (PSL) values deposited by ions from different species and different energies differ because PSL values are related to the dose deposited in the IP. Therefore, our novel configuration allows the PSL to act as an additional identifier of the ion species, providing conclusive proof that the accelerated ions are indeed silver. Details of the ion verification method are described in Appendix A.

Figure 3(b) shows the spectra of highly charged silver ions (L-shell, $Z^* = 38$–45) detected with the TP for targets with thickness of 50, 300, and 500 nm, where Z^* denotes the

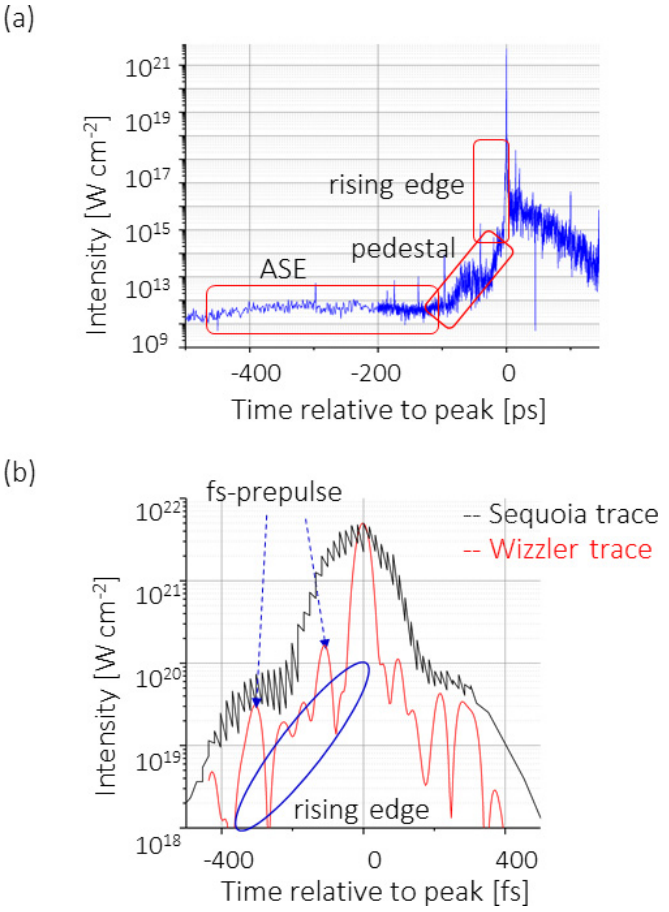

FIG. 2. (a) J-KAREN-P laser temporal profile measured by the third-order correlation technique (Sequoia). Here we call each temporal pulse shape as is shown in the figure. (b) Zoomed region around the main pulse peak. Sequoia measurement (black line) and self-referenced spectral interferometry (wizzler) (red line) with better temporal resolution.

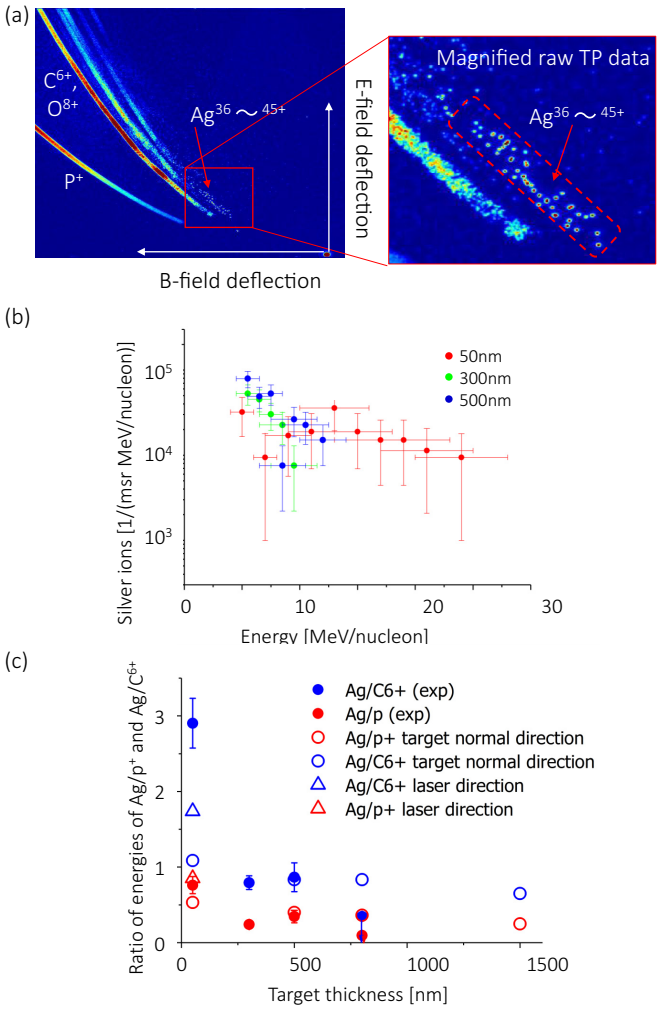

FIG. 3. (a) Imaging plate (IP) set as a detector of the Thomson parabola spectrometer placed in the target normal direction. The right-hand side shows a magnified view of the IP showing individual ion signals visible due to the small collimator size. The charge state and the energy of each silver ion track is identified by the Thomson curve with the accuracy of ±2 and ±4 MeV/nucleon at 20 MeV/nucleon. (b) *L*-shell silver ion spectra generated in the experiment. (c) Ratio of the maximum energy of silver ions and that of fully stripped carbon (blue circles) or proton (red circles). The filled and open circles show the ions accelerated in the target normal direction obtained in the experiment and simulation, respectively. The open triangles show the ions accelerated in the laser direction obtained in the simulation. For 800 nm, the silver maximum energy was set as the detection limit as no ions were observed.

ionization charge state. The highest maximum energy of the silver was found for the 50 nm target [$26(\pm^{5}_{4})$ MeV/nucleon with $Z^{*} = 45(\pm^{2}_{2})$], decreasing for 300 and 500 nm foils to $\gtrsim$10 MeV/u, with $Z^{*} \sim 40$. For the 800 nm target we could not unambiguously observe any signal from silver ions in the energy range above the detection limit of 5 MeV/nucleon, setting an upper limit on the silver ion energies. However, in the energy range of 5 to 10 MeV/nucleon we observe higher silver flux with the 300 and 500 nm targets than for 50 nm.

At the same time, the observed proton maximum energies on the RCF gradually decreased from ~47 MeV for an 800 nm target to ~35 MeV from a 50 nm target. Target thicknesses greater than 500 nm resulted in proton beams with smooth spatial distributions along target normal indicating that the acceleration mechanisms for the thicker target is dominated by TNSA, which is also supported by the fact that no transmitted light through the target is observed. However, for thinner targets, the spatial uniformity of the proton beam worsened considerably, suggesting laser-prepulse-driven pre-expansion of the rear surface or a different acceleration mechanism.

Figure 3(c) shows the ratio between the maximum energies of silver and protons, and silver and C^{6+}, indicated by red and blue points respectively, where the proton energies are the maximum observed on the RCF stack, and the silver and carbon energies are taken from TP dataset. The error bars are due to error in the estimation of the maximum energies in the TP and RCF. As the target thickness decreases, the ratio of silver ion energy to contaminant energy clearly increases.

III. IONIZATION MECHANISMS FOR ACCELERATED HIGHLY CHARGED SILVER IONS

Having experimentally demonstrated the existence of highly charged, high-energy silver ions, we can theoretically

estimate how such high charge states are achieved. It is challenging to fully ionize high Z materials, such as gold or silver, as inner shell electrons are bound in deep potential wells, i.e., a silver atom has an ionization potential $I_p >$ 5 keV for its L-shell and ∼30 keV for its K-shell. The total ionization potential density (pressure) of solid silver is $P_{\rm ion} \sim$ 1.3 peta-Pascal (PPa). A petawatt-class laser focused to an intensity $I = 10^{21}$ W/cm^2 has an energy density of 33 PPa, exceeding the total ionization potential density of solid silver. The electric potential of this intensity is 8.7 kV in electron orbital scale, i.e., $E_L = 8.7$ kV/Å where E_L is the laser electric field strength. This potential is greater than the ionization potential I_p for the L-shell of silver. For these reasons, laser light with intensity of 10^{21} W/cm^2 can strip L-shell electrons of high Z materials.

There are three relevant ionization processes in the relativistic intensity laser matter interaction: field ionization, collisional ionization, and photoionization. The dominant process for the ionization of ions which are accelerated from the target can vary depending not only on the laser parameters but also target thickness [Figs. 4(a) and 4(b)]. Here we consider the ionization mechanisms dominating in the TNSA (i.e., >500 nm target in the experiment), where we observe ≳10 MeV/nucleon silver ions with charge state of up to ∼40+ in the experiment.

A laser intensity of 5×10^{21} W/cm^2, corresponding to the experiment, is equivalent to an electric field $E_L = 20$ kV/Å, and hence is capable to field-ionize the L-shell electrons of silver atoms [29]. Because the laser field cannot penetrate through to the rear of the target, laser field ionization plays a small role for creating highly charged high-energy ions accelerated from the rear sheath. The sheath field at target rear also contributes to the ionization of the bulk ions. However, the maximum sheath field strength achieved by this laser intensity is estimated to be 14 kV/Å, i.e., about 70% of the laser electric field, at maximum (see Appendix B). Due to the large divergence of the hot electrons, the sheath strength is expected to be a few times less than the maximum value, and thus, an ionization state exceeding 40+ is unlikely to be reached by field ionization in the sheath.

Laser pulses with relativistic intensities drive hot electrons at nearly the speed of light and with a total current at the megaampere (MA) level. The hot electron current density j_H is almost neutralized by the return current density j_R consisting of the background electrons. In a solid target, the hot electron current streams freely without being perturbed by collisions, while the return current is highly collisional. Therefore, the target can be heated resistively by the return current, i.e., Joule heating. The change in bulk temperature T_e due to the Joule heating is given by

$$\frac{3}{2}\bar{n}_e \frac{\partial \bar{T}_e}{\partial \bar{t}} = \bar{\chi}\bar{j}_H^2, \tag{1}$$

where $\bar{n}_e$ is the bulk electron density normalized by the critical density $n_{\rm cr}$, $\bar{T}_e$ is the bulk electron temperature normalized by $m_e c^2$, $\bar{t}$ is the time normalized by the laser oscillation period, and $\bar{j}_H$ is the current normalized by $en_{\rm cr}c$ [30]. The normalized resistivity in the Spitzer regime [31] is given as $\bar{\chi} = \bar{\chi}_0 Z^* L/\bar{T}_e^{3/2}$, where L is the Coulomb logarithm, and $\bar{\chi}_0 = e^2\omega_L/m_e c^3$. Here, we estimate the bulk electron temperature at the target rear by assuming a stationary current with normalized hot electron density $\bar{n}_H = \eta_2\gamma$, $\bar{j} = \eta_1\gamma$ where γ is the relativistic factor of hot electrons which we here estimate based on the ponderomotive scaling [32] as $\gamma = (1 + \eta_1 a_0^2/2)^{1/2}$ with the conversion efficiency from the laser to hot electrons η_1. Here, $\eta_2 = \pi r^2/\pi(r + l\tan\theta)^2$ is the geometrical factor to take into account the electrons' divergence and the resulting current density reduction, defined as the ratio of hot electron beam size at the source point to that at the target rear, where r, l, and θ are the focal spot radius, distance from the source point to the target rear surface, and the half angle of the electrons' divergence, respectively. Integration of

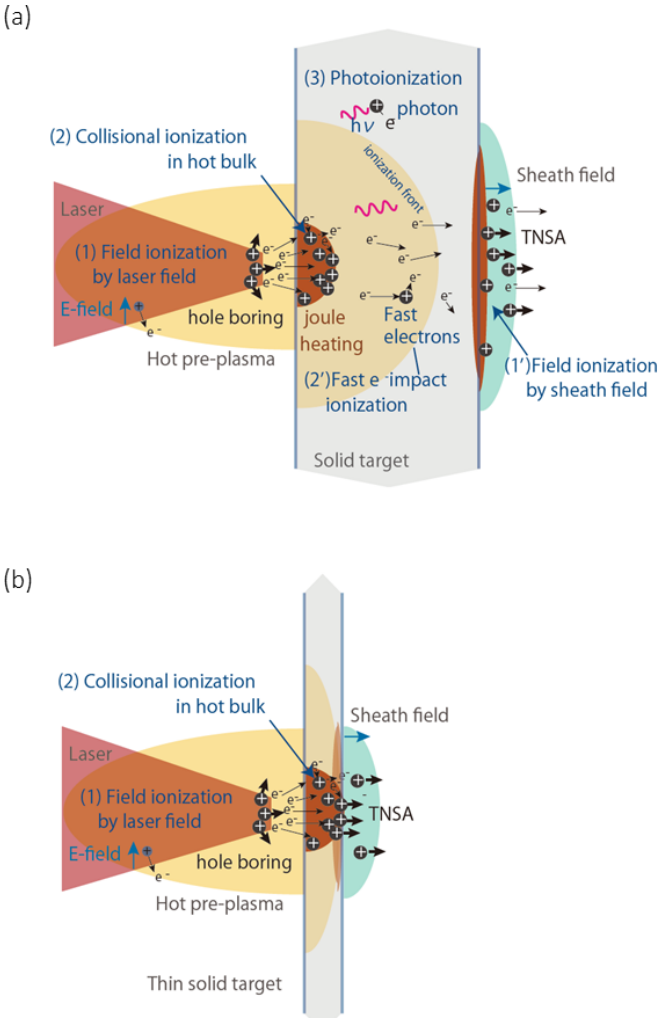

FIG. 4. Diagrams showing contributing ionization mechanisms for (a) thick and (b) thin solid targets. (a) For thick targets, field ionization can occur at the front of the target in the laser fields and also at the sheath field at the back of the target, where the ions are also accelerated by the sheath. There is a highly charged region created via collisional ionization from fast electron collisions and Joule heating, however, the ionization state reduces with depth into the target. (b) For a thin target, the highly charged region reaches to the rear of the target and contributes to ionizing ions there to higher charge states than possible by the sheath field. These highly charged ions are then accelerated to high energies in the sheath.

Eq. (1) gives

$$\bar{T}_e \sim \left(\frac{(\eta_2\gamma)^2\bar{t}}{\bar{n}_i}\right)^{2/5}, \tag{2}$$

neglecting the initial electron temperature. Here, $\bar{n}_i$ is the normalized bulk ion density. By setting $a_0 = 50$, $\eta_1 = 0.6$ from the simulation described later, $\bar{n}_i = 35$ as the solid, and $\bar{t} = 17$ as the pulse duration, we obtain $\gamma = 27$. The geometrical factor is $\eta_2 = 0.72$ by assuming r, l, and θ as 1μm, 0.5μm, and 20 degrees, respectively. The bulk electron temperature is then calculated to be $T_e \simeq 8$ keV. Note here that electrons with keV energies thermalize in the time scale of fs in a solid silver target. With the electron temperature of 8 keV, about 30% of the electrons have energies exceeding 10 keV. Electrons with such energies can ionize silver ions via collisions to charge states higher than 38+ [33].

The dominant ionization process for the ions extracted out of the target depends on the target thickness as illustrated in Fig. 4(a) and 4(b). For a thick target (a), the ions extracted by the TNSA acceleration are ionized by field ionization in the sheath field. Although a strong ionization by the laser field produces highly charged ions at the laser front, they have a large divergence due to the small laser focal spot. Also, the number of the ions is not significant since the process occurs in the low density preplasma. There is a highly charged region created via collisional ionization, however, it is not exposed to the rear-side sheath field. However, if the target is thin enough, the sheath field overlaps with the highly charged bulk region, resulting in acceleration of the high-Z ions as shown in (b). This target thickness dependency is consistent with the experiment, in which high-Z acceleration was measured for targets of thickness 500 nm, but not above.

When fast electrons pass through the high-Z target they also emit hard x rays and γ rays, which can photoionize the target. Based on the low cross section for the photoionization [34] to overcome the energy band between Ag^{37+} to Ag^{38+}, and the conversion efficiency from the laser to hard x-ray/gamma-ray photons being $<1\%$ at laser intensities $\leqslant 10^{22}$ W/cm^2 [35,36], photoionization is negligibly small compared to other processes in these conditions.

IV. EFFECT OF FINITE RISING-EDGE OF THE LASER PULSE; DETACHMENT OF THE CONTAMINANT LAYER

Contaminants on the target surface, which contain water and hydrocarbons, typically prevent the acceleration of even highly ionized bulk ions. The lighter contaminant ions are the first to be exposed to the sheath field and accelerated in the field potential, shielding the electric field experienced by the bulk ions and, therefore, reducing their final energies. To address this problem, several target cleaning techniques have been reported, including Joule heating [22,37], ablation by CW or short-pulse lasers [17,18,20,38,39], etching by an ion sputter gun [40,41], and self-cleaning by the main laser pulse in relativistically transparent plasma [42].

However, as we will show, contaminants are also preferentially accelerated by the unavoidable intense picosecond (ps)-scale rising edge of the laser pulse, which varies significantly from an ideal Gaussian pulse [Figs. 2(a), 2(b), and 5]. It has been shown that this rising edge suppresses proton acceleration [43–45], due to pre-expansion of the target rear surface. However, no previous studies focused on the positive impact on bulk ion acceleration. In optimal conditions, the contaminant layer can pre-expand and effectively detach from the target without significantly pre-expanding the bulk, resulting in the target ions being exposed to stronger sheath fields and accelerated to higher energies.

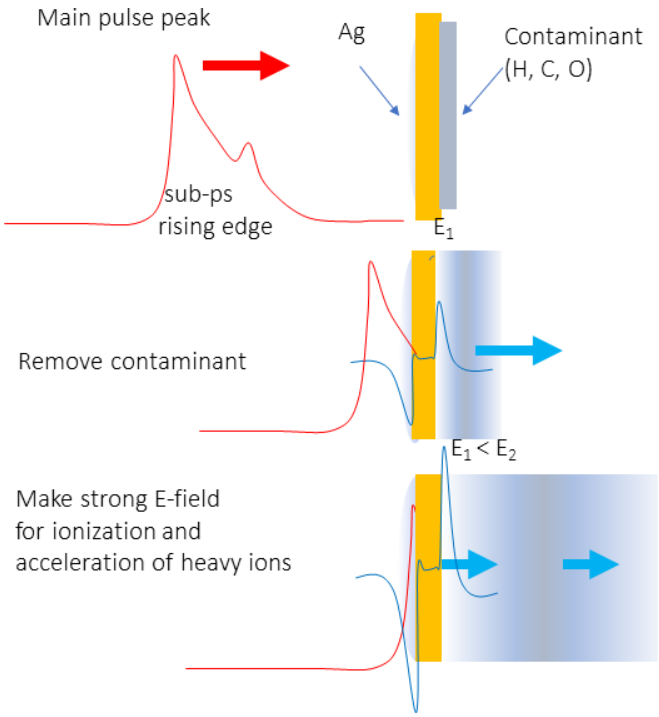

FIG. 5. Illustration showing the sheath-field generation at the target rear by the rising edge and main pulse and the process for removing contaminants.

The contaminant layer is assumed to have an initial thickness of $l_{\rm cont} = 5$ nm [40] and electron density $n_{\rm cont} = 100 n_{\rm cr}$. During the interaction with the rising edge, the contaminant layer expands to an approximate spatial scale of $L = C_s t$ where $C_s = (Z^* k_B T_H / M_i)^{0.5}$ is the sound speed, and k_B, T_H, and M_i are the Boltzmann constant, hot electron average energy, and ion mass, respectively.

A sheath field is excited at the position where the electron density becomes lower than the fast electron density $n_H \sim \gamma n_{\rm cr}$, where the fast electron current can no longer be neutralized by a return current. We define a "detachment" criterion as when the contaminant layer, of initial thickness and density of $l_{\rm cont}$ and $n_{\rm cont}$, respectively, expands to a characteristic length $l_{\rm eff}$, the spatial scale at which the average contaminant layer density drops off to $\gamma n_{\rm cr}$ (i.e., $n_{\rm cont} l_{\rm cont} = \gamma n_{\rm cr} \cdot l_{\rm eff}$). The time scale of the detachment is then given by $l_{\rm eff}/C_s$. We here assume a fully ionized contaminant layer and the relativistic rising edge with $a_0 \geqslant 1$. Using the ponderomotive scaling [32], the sound velocity is $C_s \geqslant 3$ μm/ps and $\geqslant 2$ μm/ps for the charge to mass ratio $Z^*/M_i = 1$ for protons and 0.5 for carbon/oxygen ions. The time scale of the detachment for $Z^*/M_i = 1$ (0.5) is then obtained as $l_{\rm eff}/C_s = 150$ (210) fs for $a_0 = 1$ as reference. For higher a_0, the time scale becomes shorter than the reference. Short pulse petawatt lasers

have unavoidable rising edges with relativistic intensities a few hundred fs before the main pulse [Figs. 2(a) and 2(b)]. Thus, the contaminant layer is effectively detached from the target, allowing the sheath field driven by the main pulse to accelerate the silver ions. Conversely, the pre-expansion of the contaminant layer is a serious impediment to acceleration of protons to energies exceeding 100 MeV, even if applying sophisticated contrast enhancing techniques such as, a plasma mirror [46], plasma shutter [47], or frequency doubling [48]. As the peak intensity gets increasingly higher in next generation high-power laser systems [49], this issue will become more significant.

V. NUMERICAL SIMULATIONS OF IONIZATION AND ACCELERATION DYNAMICS

To understand fully the difference in the ionization and acceleration mechanisms from changing the foil thickness observed in the experiment, hydrodynamic, and kinetic particle-in-cell (PIC) were carried out. The two-dimensional (2D) hydrodynamic simulations were applied to estimate the preplasma generation from the low intensity amplified spontaneous emission (ASE) and pedestal over a timescale of hundreds ps using the FLASH hydrodynamics framework in cylindrical geometry [50] with the measured J-KAREN-P laser temporal pulse [Figs. 2(a) and 2(b)]. A box of $15 \times 50\,\mu\mathrm{m}^2$ in the r and z directions, respectively, is simulated using adaptive mesh grids. A tabulated target material equation of state (EOS) is pre-computed using FEOS [51], a modification of MPQEOS [51,52]. Ionization was calculated using the Thomas-Fermi model. Thermal conduction and heat exchange are calculated using the Spitzer model. Radiation was found to be unimportant for such cool dense targets and, therefore, not included in the modeling here. The laser energy is coupled into the electron temperature using a ray tracing algorithm with the inverse bremsstrahlung model. Due to the use of cylindrical geometry, the laser was incident at target normal. The simulations were performed up to 10 ps before the peak of the intense pulse, at which point the intensity is $\sim 10^{14}\,\mathrm{W/cm}^2$, for the different target thicknesses.

Using the density profile from the hydrodynamic simulation, we simulated the laser relativistic rising edge and main pulse using the PIC code PICLS, including collisions with weighted particles [53], field and collisional ionizations [54], and radiation [55]. This allows simulation of plasma formation and energy transport for plasmas with densities ranging from preplasma to solid density. A 2D relativistic simulation was performed in Cartesian geometry with a box size of $80 \times 80\,\mu\mathrm{m}^2$ and the a grid size of 0.01 μm. Absorbing boundary conditions are used for particles in the transverse direction, representing a target with large transverse size. The laser with the experimentally measured temporal pulse shape is focused onto Ag targets at an incidence angle of 30 degree, slightly lower than the 45 degrees used experimentally due to computational constraints, and a Gaussian transverse focal spot with a diameter of 2 μm ($1/e^2$). At the rear target surface a 20 nm layer of protons and deuterons with densities of $12.5\,n_{\mathrm{cr}}$ are added to mimic the surface contaminants. Note that although the contaminant layer includes oxygen and carbon, we instead use deuterons, as the ions will be fully stripped due to the rapid ionization by the relativistic rising edge. The silver ionization state is initialized from the hydrodynamic simulation, while the plasma temperatures are zero, as the initial temperature is insignificant compared to the final temperature. We found by executing a full scale simulation that the effect of the laser rising edge between -10 to -2 ps before the main pulse, during which laser intensity is less than $10^{16}\,\mathrm{W/cm}^2$, is negligibly small. Although the preplasma is heated to a few eV, it does not expand significantly over this timescale. Therefore, for further calculations the PICLS simulation was started 2 ps prior to the main pulse, initialized using the density profile from the hydrodynamic simulation.

Figures 6(a)–6(c) show the ion density distribution of the hydrogen, deuterium, and silver at the time of the main pulse arrival for a 500 nm target, showing contaminants effectively detach from the target rear and moving over $\sim 2\mu$m, where the density drops below the relativistic critical density γn_{cr}. However, the silver bulk is not significantly deformed and maintains a steep density profile on the rear surface with an electron density higher than γn_{cr}. A large sheath field is, therefore, excited at the rear of the silver target, not in the detached contaminant plasma. Its strength reaches up to 52 TV/m at maximum and it takes 50 fs to decrease to 80 percent of the maximum.

Figures 6(d)–6(f) show the proton, carbon and silver energy spectra for 50, 500, and 1500 nm targets along the target normal direction in the upper row (i.e., $\pm$ 10 degrees from the target) and along the laser direction in the lower row ($\pm$10 degrees from the laser propagation direction). The maximum proton energies were higher ($\sim$55 MeV) with thicker targets (500 and 1500 nm) than the 50 nm target ($\sim$45 MeV). The proton flux at higher energy range (>30 MeV) is highest with the thickest target. It is well known that 2D PIC simulations overestimate ion energies, therefore, we instead rely on the comparison of the ratio of maximum eneriges between silver and proton (C6+) accelerated toward target normal direction [shown by open circles in Fig. 3(c)]. The tendency seen in simulation matches well to that seen in experiment, confirming that proton acceleration can be suppressed due to predetachment of the contaminant layer which is more pronounced for thinner targets [Fig. 3(c)]. The L-shell silver ions ($Z^* \geqslant 38$) are accelerated to <20 MeV/nucleon for 1500 and 500 nm targets. The experimentally observed silver ion spectra for the 500 nm case closely match the simulation, although for the thickest case (800 nm) they do not, i.e., at least no energetic silver ions (>5 MeV/nucleon) are observed. The difference can be explained by the assumption of contaminant layer thickness in the simulation, which was not measured in the experiment. The simulation also shows that the majority of the ions of all species and charge states are accelerated toward the target normal direction when the target thickness >500 nm [Figs. 6(e) and 6(f)], as expected for TNSA. However, for a 50 nm target, the highly charged ($Z^* > 30$) silver ions are accelerated to $\sim$30 MeV/nucleon and $\sim$40 MeV/nucleon in target normal and laser directions, respectively [Fig. 6(d)]. This distinct difference for the thinnest target (50 nm) indicates an acceleration mechanism modified from simple TNSA.

Ions can also be generated from the front surface of a laser-solid interaction [56–60]. Figures 7(a) and 7(b) show the phase space distribution of the accelerated ions for the 500 nm

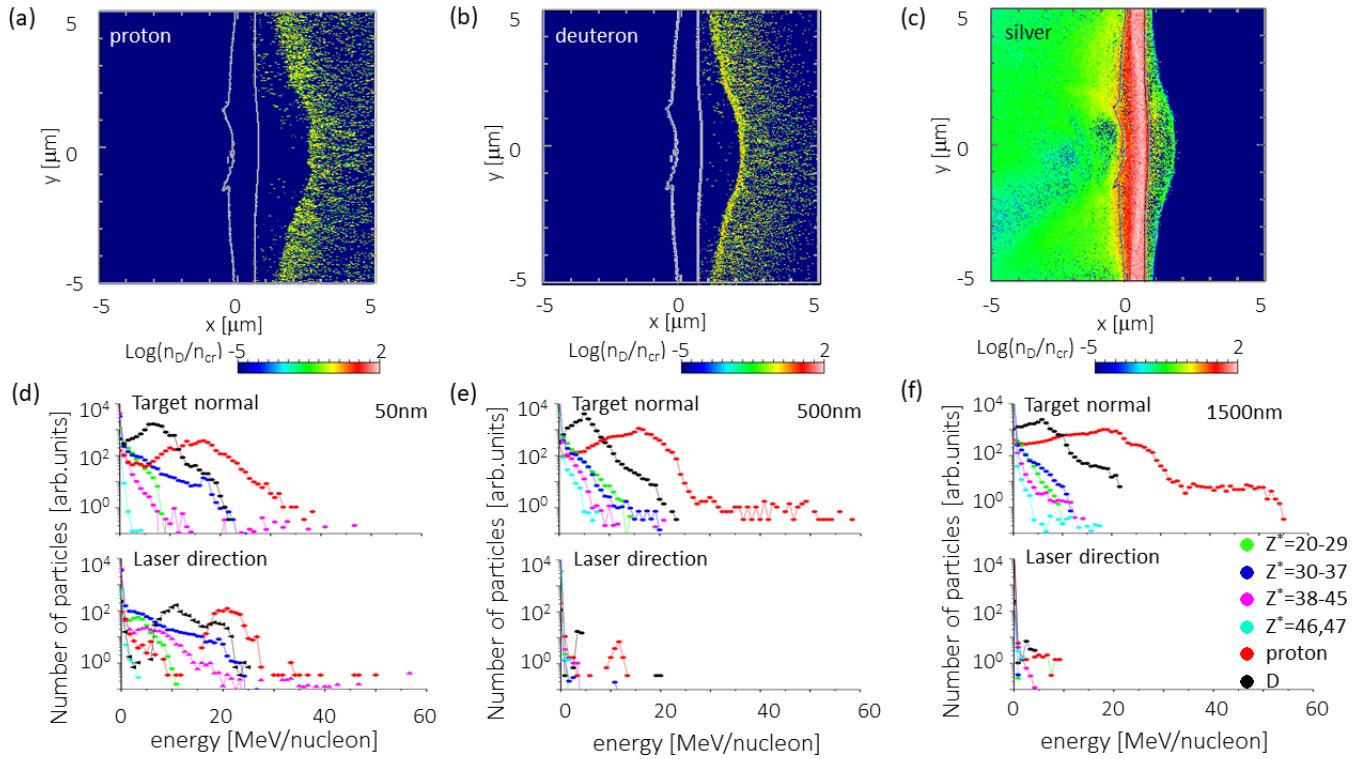

FIG. 6. Density distribution of the protons (a), deuterons (b), and silver ions (c) at the peak of the main pulse for 500 nm target. The laser focuses at $(x, y) = (0, 0)$. Energy spectra of the silver ions with different charge states for (d) for 50 nm, (e) for 500 nm, and (f) for 1500 nm targets. The upper and lower rows show the spectra of ions emitted from the rear side of the target in the target normal direction (-10 degrees $< \theta <$ 10 degrees), and those toward the laser direction (20 degrees $< \theta <$ 40 degrees), respectively, where θ is the angle from the target normal.

target at the main pulse peak, where x and y are directions perpendicular and parallel to the target, respectively, and u denotes the ion velocity. There are two separated distributions in the x-u_x distribution in Fig. 7(a) corresponding to that of front-side and rear-side accelerated ions. The maximum energies of the ions from the front side is smaller than these from the rear side. The ions originating from the rear side have larger number density than these from the front side [Fig. 7(b)]. Therefore, the ions detected by the TP, especially in the higher energy range, are mainly originating from the target rear side, i.e., collisionally ionized by electrons in the target bulk and extracted out by the rear-side sheath.

To understand the dominating ionization mechanism for generating highly charged high-energy silver ions, the ionization process of each particle in the PIC simulation is tracked, and its final ionization event is recorded. The resulting spectra of the silver ions [Figs. 8(a)–8(c)] that were field ionized as the last ionization event are shown in the upper row, and those

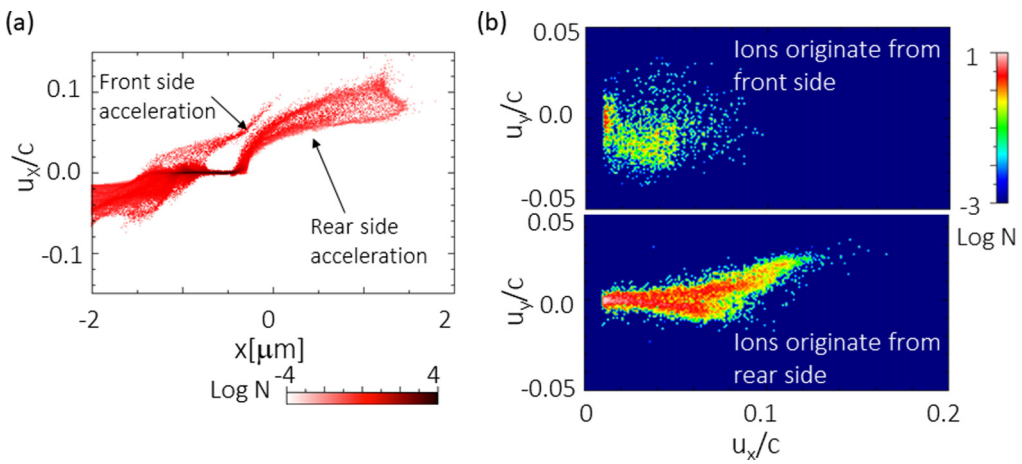

FIG. 7. Phase space plot of the silver ions in (a) $x - u_x$ and (b) $u_x - u_y$ planes where u is the ion velocity for the 500 nm target. (b) Upper (lower) panels show those of ions originating from front (rear) side of the target.

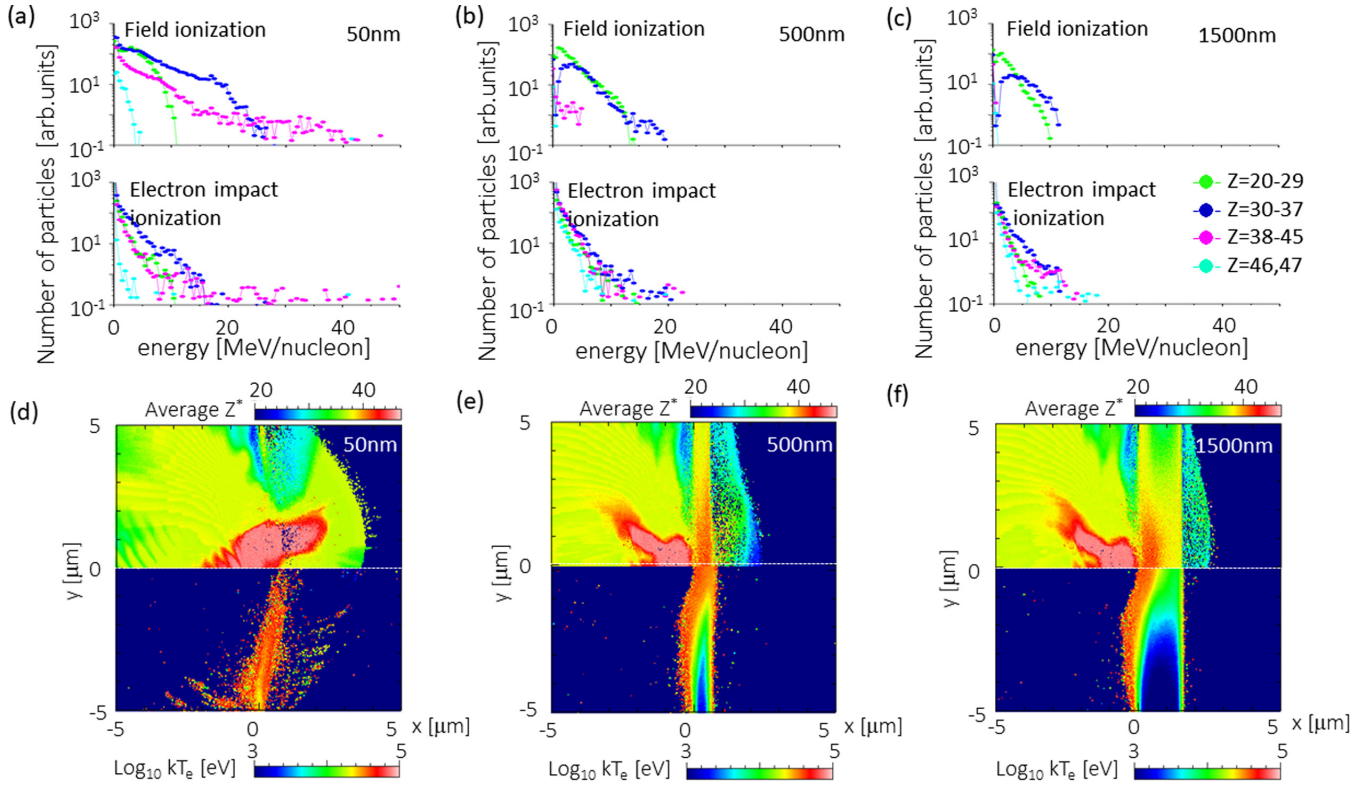

FIG. 8. Spectra of silver ions with momentum $p_x > 0$ (a) for a 50 nm target, (b) for a 500 nm target, and (c) for a 1500 nm target. Those in the upper (lower) row are ions whose last ionization was due to field (electron impact) ionization. Average charge state distributions (upper) and temperature distribution in the target (lower) for (d) 50 nm, (e) 500 nm, and (f) 1500 nm, showing the time 35 fs after the main pulse peak.

that were collisionally ionized as the last ionization event are shown in the lower row for 50, 500, and 1500 nm foils, respectively. Although for lower charge states ($Z^* < 38$) the ions can be either field or collisionally ionized, for targets thicker than 500 nm, the dominating ionization mechanism for high-energy L-shell ($Z^* = 38$–45) and K-shell ($Z^* = 46$–47) silver ions is collisional ionization, while that for the thinnest target (50 nm) is field ionization, albeit with a significant contribution from collisional ionization.

Figures 8(d)–8(f) show the average silver charge state (upper) and bulk electron temperature distribution (lower) 35 fs after the main pulse arrival for 50, 500, and 1500 nm targets, respectively. Here the bulk temperature is obtained by averaging electrons with energies below 100 keV. Regions with no electrons or where all electrons exceed 100 keV are set to zero temperature. For all target thicknesses, the temperature of the bulk of the target rises to >10 keV, consistent with the theoretical prediction for the electron temperature via resistive heating, and sufficient to collisionally ionize the silver ions up to L-shell, which are observed in the experiment. As was described in Figs. 4(a) and 4(b), the thickest target has a lower temperature at the rear surface resulting in a lower charge state [Fig. 8(f)], and also a weaker sheath field due to the geometrical reduction in the hot electron density at the rear surface, resulting in a reduction in the accelerated silver energies, also consistent with the experimental results.

However, the conditions differ drastically for the 50 nm target case. As is shown in Figs. 9(a) and 9(b), the 50 nm target is strongly expanded by the prepulses and rising edge well before the main pulse arrives, although still initially opaque to the laser [Fig. 9(c)]. Using such a thin target results in an increase in the sheath field strength [Fig. 9(d)], due to reduced geometrical expansion of the fast electrons, increased recirculation [35] and also an increase of the laser to electron conversion efficiency at the critical surface because of the longer plasma scale length compared to the thicker targets. However, the sheath strength is still insufficient to reach the highest ionization states through field ionization, as shown in Fig. 8(a), meaning that these must instead be ionized by the laser field directly.

The reduced density also contributes to the high-energy silver ion acceleration due to the photon pressure at the front surface, as shown in [Fig. 9(a)]. The hole boring (HB) speed of the main pulse through the solid silver target can be estimated as $v_{\mathrm{HB}} \approx [I/(M_i n_i c)]^{1/2}$ [3,61]. By assuming a silver density $n_{\mathrm{Ag}} = 3n_{\mathrm{cr}}$ [Fig. 9(c)] and a laser intensity of 5×10^{21} W/cm^2, the hole boring velocity is $v_{\mathrm{HB}} \sim 700$ nm/40 fs. Since the initial thickness of the region with electron density over γn_{cr} is about 660 nm assuming an average charge state of 40+, the main pulse can drill through the target and break out the rear side as shown in Fig. 9(b). The silver ions ($Z^* > 30$) ionized by the laser field are pushed volumetrically by the HB process and injected into the strong sheath field, resulting the efficient acceleration. The target eventually becomes relativistically transparent [Fig. 9(b)], just after the main peak of the pulse, which is also confirmed by the transmitted light measured in the experiment.

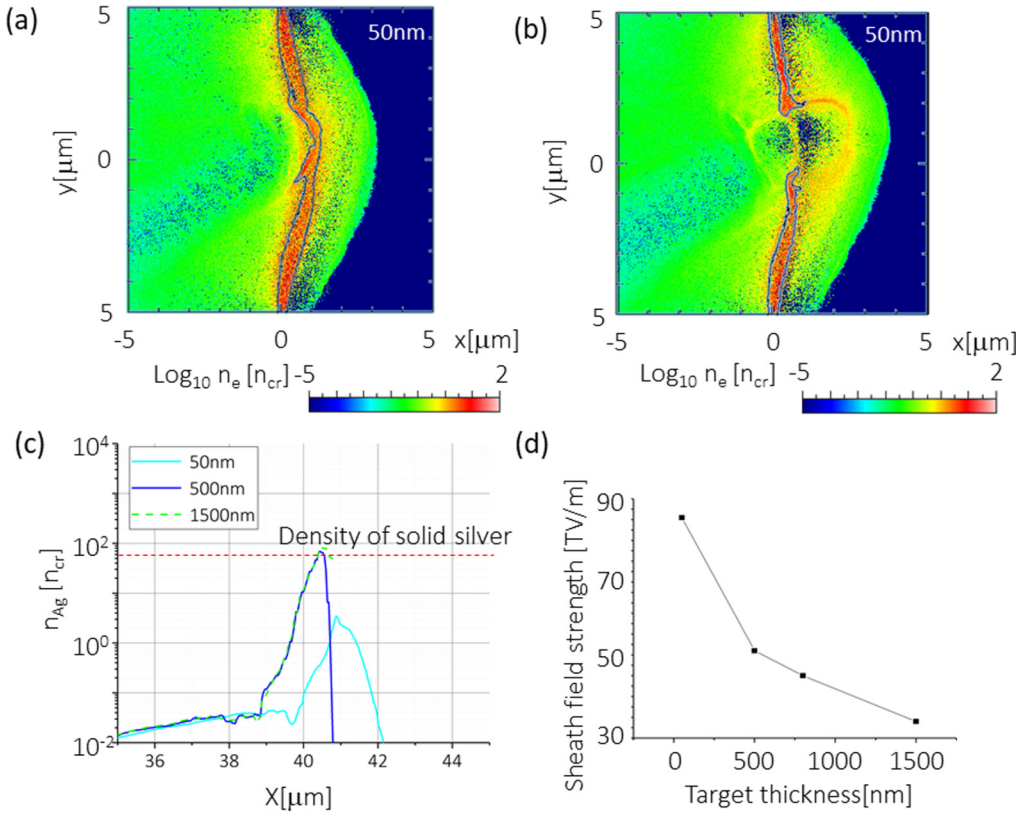

FIG. 9. Electron density profile in the PIC simulation for the 50 nm target at the time of (a) just before the main pulse irradiation and (b) 35 fs after the main pulse irradiation. The black lines shown in both panels indicate the position with density of $\gamma n_{\rm cr}$. (c) Lineout of the initial silver density profile for the PIC simulation provided by the hydrodynamic simulation for each thickness of targets, i.e., light blue, blue, and dotted green show the cases of 50, 500, and 1500 nm targets, respectively. Initial position of the target front surface is located at $X = 40$. The laser is irradiated from left-hand side to the target. (d) Sheath field strength from the PIC simulation against target thickness.

Even though we observe highly charged high-energy silver ions from the 50 nm target, the transition of the dominant acceleration scheme from TNSA to HB + TNSA is strongly dependent on the rising edge of the main pulse, which is not easy to control even for state-of-the-art PW-class lasers. A small change in target thickness or laser rising edge can significantly change the interaction and generated ion beam. Thus, for a stable source of highly charged high-energy ions with a good collimation, using a slightly thicker target and relying on the collisional ionization and extraction by the TNSA may be optimal for many applications.

It may be possible to further optimize the beam by using a thin higher-Z substrate, such as Au, with an ultrathin silver layer, allowing the use of a reduced target thickness with improved resistance to the rising edge and prepulses to maximize rear sheath electron density in the TNSA regime. It is also noted that if the relativistic rising edge in PW-class laser pulses cannot be removed appropriately, the removal of the contaminant layer on the target by existing techniques [17,18,22,27,37–42] may actually impede higher energy ion acceleration, as the contaminant acts as a sacrificial layer preventing the pre-expansion of the target bulk.

VI. CONCLUSION AND OUTLOOK

To conclude, we have investigated and elucidated the dynamics of ultra-intense laser-driven heavy-ion acceleration. Highly charged high-energy silver ions were accelerated by a short pulse petawatt class laser interacting with a silver target with optimum thickness (500 nm), with ionization being dominated by electron collisional ionization inside the target, which is heated to over ∼10 keV by high-intensity short laser pulses. However, for the higher energy silver ions generated by the thinnest targets, the dominant ionization process shifts to field ionization by the laser. In this case, the acceleration is the combination of hole boring driven by photon pressure at the target front- and the rear-side sheath field acceleration.

This comprehensive understanding of laser-driven heavy-ion acceleration dynamics paves the way to controlling the production of highly charged high-energy heavy-ion beams with PW class high-intensity short-pulse lasers. At the same time, we have shown that the existence of rising edge and prepulses will be a serious impediment toward achieving higher energy proton beams using high-intensity laser pulses from PW-class and/or future laser systems [49,62] without careful consideration. The ability to accelerate high charge state heavy ions over such small spatial and temporal scales is a significant step toward the realization of a next-generation

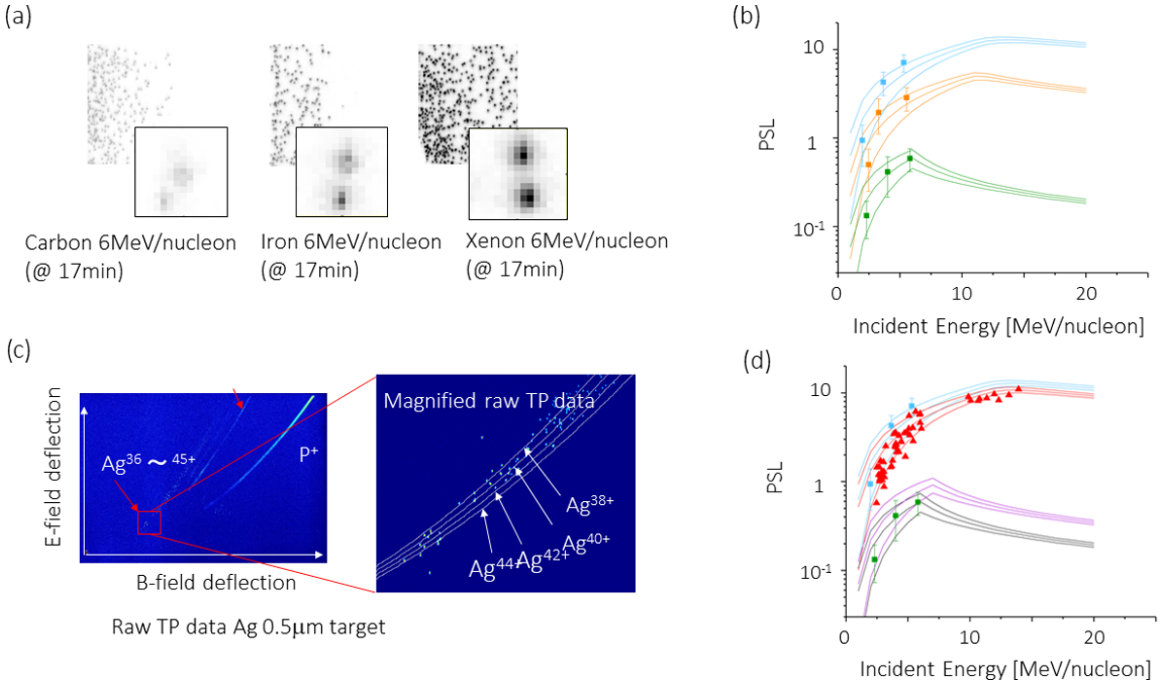

FIG. 10. (a) Signal due to individual carbon, iron, and xenon ions, all with 6 MeV/nucleon as recorded on the imaging plate (BAS-SR2025). (b) PSL values depending on the incident energies of the ions. Blue, orange, and green data points are those of Xe, Fe, and C ions, respectively, from a conventional accelerator. Overlapped solid lines are the best fit of the Birks formula shown in the text and the error range within 1 s.d. level. (c) Raw IP data for the TP measuring laser-driven silver ions. Clear parabolas are observed. Silver ions are recorded as "pixelized" tracks (right-hand side magnified image). The brightness of the tracks originated from silver ions and those from oxygen ions are clearly different. (d) Same data points for Xe and C as is shown in panel (b) but with the data points from silver ion tracks accumulated from the laser experiment accumulated from IP shown in panel (c) (red dots) and prediction of PSL value for silver (red line) and oxygen (purple line) with error range of 1 s.d.

compact heavy-ion accelerator, which will enable exploration at the frontier of nuclear physics and nuclear astrophysics.

ACKNOWLEDGMENTS

We are grateful to the J-KAREN-P operation team for their support. This work was partially supported by JST-Mirai Program Grant No. JPMJMI17A1, Japan. M.N. was supported by JST PRESTO Grant No. JPMJPR16P9 and Kakenhi Grant No. 16K05506. M.N. was supported by QST President's Strategic Grant(QST International Research Initiative (AAA98) and Creative Research (ABACS). M.N. and N.P.D. were supported by JSPS Post-doctoral Fellowship and Kakenhi Project No. 15F15772, M.N. and H.S. were supported by Mitsubishi Foundation (ID:28131). N.I. and Y.S. are supported by JSPS KAKENHI Grant No. JP15K21767. N.I. was also supported by the Foundation for the Promotion of Ion Engineering. M.H. was supported by JSPS Kakenhi Grants No. JP17J02020 and No. JP19KK0072. This work is partially performed on "Plasma Simulator" (FUJITSU FX100) of NIFS with the support and under the auspices of the NIFS Collaboration Research program (NIFS17KNSS090). T.A.P., M.A.A., and A.Ya.F. were supported by the state assignment of FASO of Russia to JIHT RAS (Topic No. 01201357846). FLASH was in part developed by the DOE NNSA-ASC OASCR Flash Center at the University of Chicago.

APPENDIX A: METHOD FOR DISCRIMINATING SILVER IONS

To unambiguously determine that the tracks in the silver trace were silver and not another contaminant ion with lower atomic number, we performed an extensive calibration experiment of the imaging plate (IP) detector using a conventional accelerator, HIMAC, at NIRS, Japan. The photo stimulated luminescence (PSL) values of ions from different species (different Z, such as C, Fe, and Xe) and three different energies (2, 4, and 6 MeV/nucleon) were investigated. The resolution of the scanner was set to be $50 \times 50\,\mu\text{m}^2$, which hereafter is referred to as a pixel. Each track is recorded in multiple pixels. Tracks originating from different species with same energies show different brightness as shown in Fig. 10(a).

PSL values of 49 pixels (7×7) around a pixel which has local maximum PSL value are accumulated to obtain the PSL value of each track. After taking into account the well-known IP (imaging plate) fading effect, PSL values of tracks caused by different ion species with different energies are plotted in Fig. 10(b). Each data point in the figure shows the average PSL value and error range of 1 s.d. statistically accumulated from more than 100 tracks. These data points are fitted to the Birks formula,

$$Q(Z, E_0) = \int_0^x dx \, \frac{S\,dE/dx}{1 + kB\,dE/dx}, \tag{A1}$$

where S, kB, and dE/dx are the efficiency in scintillation, quenching effect and stopping power respectively [63]. $Q(Z, E_0)$ is the amount of light output from the scintillation material in the IP in the unit of PSL, which depends on the incident energy and atomic number of ions. The integral in Eq. (A1) is numerically carried out by using the values of dE/dx on the imaging plate (SR2025) calculated by using the PHITS code [64] including the ATIMA model [65]. In the fitting, the free parameters are S and kB and the best fit parameters are $(8.0 \pm^{0.2}_{0.5}) \times 10^{-3}$ [PSL MeV^{-1}] and $(0.0018 \pm^{0.0062}_{0.0018})$ [μm MeV^{-1}], respectively, with a 68% confidence level.

From Fig. 10(b), it is clear that the method enabled the discrimination of different ion species depending on the recorded dose of each track made by each ion, overcoming the weakness of the ion spectral measurements by the TP in which ions of different species but the same charge to mass ratio overlap on the same TP curves. Figure 10(c) shows the IP image of the laser-plasma experiments. Here the difference in the brightness of the tracks from different species like silver and oxygen (carbon) are also clearly seen. In Fig. 10(d), the same data of Xe and C as in Fig. 10(b) are shown together with the PSL values of the tracks which fall on the TP parabola trace having 36+ to 45+ charge state of silver which are accumulated from J-KAREN-P laser shots using a 500 nm silver target (red triangles). The red and purple solid lines show the prediction of the PSL values for Ag and carbon estimated from the Birks formula using the best-fit parameters from our calibration shown above. The majority of the possible contaminant ion species on the target are oxygen and carbon from the contaminant layer on the target surface. The PSL values of the contaminant species are far lower than the PSL values of the tracks from the Ag target shots. Therefore, we can conclude that those tracks (red triangles) are caused by silver ions.

APPENDIX B: FIELD IONIZATION BY THE SHEATH FIELD

To understand the role of the sheath field in the ionization of the heavy ions at the target rear, we first develop a simple analytical model to estimate the strength of the rear-side sheath field. Energy flux conservation from the absorbed laser to hot electrons at the laser-plasma interface is $\eta_1 I = cn_H k_B T_H$, where the flow velocity of the hot electrons is approximately the speed of light c, I is the laser intensity, η_1 is the conversion efficiency from the laser to hot electrons, k_B is the Boltzmann constant, and n_H and T_H are the hot electron density and temperature, respectively.

At the target rear, the hot electrons create a sheath electric field E_s whose peak amplitude is estimated by $eE_s = k_B T_H/\lambda_D$ [66]. Here $\lambda_D = (k_B T_H/(4\pi n_s e^2))^{1/2}$ is the Debye length, where e is the elementary charge, and n_s is the hot electron density at the target rear. To estimate n_s, we introduce a geometrical factor to represent the spatial expansion of the electrons during the transport from the laser absorption point to the rear side of the target. Namely, we connect the hot electron densities on the front side and rear side via $n_s = \eta_2 n_H$ where η_2 is defined as the ratio between the area of the focal spot and the sheath area at the target rear, $\eta_2 = \pi r^2[\pi(r + \ell \tan\theta)]^{-1}$ where r, ℓ, and θ are the focal spot radius, distance from the laser absorption point to the target rear surface, and the half angle of the electrons' divergence, respectively. The sheath field is then given by $eE_s = (4\pi e^2 \eta_2 n_H k_B T_H)^{1/2}$. Using the relation $I/c = (eE_0)^2/[2(m_e c\omega_L)^2]$, we obtain

$$E_s = E_0\sqrt{\frac{\eta_1\eta_2}{2}}, \tag{B1}$$

where $n_{\rm cr} = m_e\omega_L^2/(4\pi e^2)$ is the critical density, m_e is the electron rest mass, ω_L is the laser frequency, and E_0 is the laser electric field amplitude. Equation (B1) indicates that the sheath field strength is proportional to that of the laser field and the maximum value is given by $E_s = E_0/2^{1/2}$ for $\eta_1 = \eta_2 = 1$, i.e., about 70% of the laser amplitude. Due to the finite divergence of the hot electrons, the sheath strength is expected to be a few times less than the maximum value. Note that the considered interaction is for a tight focus laser where the hot electron recirculation [66] is not significant.

[1] P. Drake, *High Energy Density Physics* (Springer, Berlin, 2006).

[2] D. Habs, G. Pretzler, A. Pukhov, and J. Meyer-ter-vehn, Laser acceleration of electrons and ions and intense secondary particle generation, Proc. Part. Nucl. Phys. **46**, 375 (2001).

[3] S. V. Bulanov, J. J. Wilkens, T. Zh. Esirkepov, G. Korn, G. Kraft, S. D. Kraft *et al.*, Laser ion acceleration for hadron therapy, Phys. Usp. **184**, 1265 (2014).

[4] M. Roth, T. E. Cowan, M. H. Key, S. P. Hatchett, C. Brown, W. Fountain, J. Johnson, D. M. Pennington, R. A. Snavely, S. C. Wilks, K. Yasuike, H. Ruhl, P. Pegoraro, S. V. Bulanov, E. M. Campbell, M. D. Perry, and H. Powell, Fast Ignition by Intense Laser-Accelerated Proton Beams, Phys. Rev. Lett. **86**, 436 (2001).

[5] T. Esirkepov, M. Borghesi, S. V. Bulanov, G. Mourou, and T. Tajima, Highly Efficient Relativistic-Ion Generation in the Laser-Piston Regime, Phys Rev. Lett. **92**, 175003 (2004).

[6] I. A. Maltsev, V. M. Shabaev, I. I. Tupitsyn, A. I. Bondarev, Y. S. Kozhedub, G. Plunien, and T. Stohlker, Electron-positron pair creation in low-energy collisions of heavy bare nuclei, Phys. Rev. A **91**, 032708 (2015).

[7] M. Nishiuchi, H. Sakaki, T. Zh, K. Nishio, T. A. Pikuz, A. Ya. Faenov *et al.*, Acceleration of highly charged GeV Fe ions from a low-Z substrate by intense femtosecond laser, Phys. Plasmas **22**, 033107 (2015).

[8] M. Nishiuchi, H. Sakaki, T. Zh. Esirkepov, K. Nishio, T. A. Pikuz, A. Ya. Faenov *et al.*, Toward a novel laser-driven method of exotic nuclei extraction-acceleration for fundamental physics and technology, Plasma Phys. Rep. **42**, 327 (2016).

[9] S. Busold, D. Schumacher, C. Brabetz, D. Jahn, F. Kroll, O. Deppert, U. Schramm, T. E. Cowan, A. Blažević, V. Bagnoud, M. Roth, Toward highest peak intensities for ultrashort MeV-range ion bunches, Sci. Rep. **5**, 12459 (2015).

[10] S. C. Wilks, A. B. Langdon, T. E. Cowan, M. Roth, M. Singh, S. Hatchett *et al.*, Energetic proton generation in ultraintense laser-solid interactions, Phys. Plasmas. **8**, 542 (2001).

[11] E. L. Clark, K. Krushelnick, J. R. Davies, M. Zepf, M. Tatarakis, F. N. Beg *et al.*, Measurements of Energetic Proton Transport Through Magnetized Plasma from Intense Laser Interactions with Solids, Phys. Rev. Lett. **84**, 670 (2000).

[12] R. A. Snavely, M. H. Key, S. P. Hatchett, T. E. Cowan, M. Roth, T. W. Phillips, M. A. Stoyer, E. A. Henry, T. C. Sangster, M. S. Singh, S. C. Wilks, A. MacKinnon, A. Offenberger, D. M. Pennington, K. Yasuike, A. B. Langdon, B. F. Lasinski, J. Johnson, M. D. Perry, and E. M. Campbell, Intense High-Energy Proton Beams from Petawatt-Laser Irradiation of Solids, Phys. Rev. Lett. **85**, 2945 (2000).

[13] S. Kar, K. F. Kakolee, B. Qiao, A. Macchi, M. Cerchez, D. Doria, M. Geissler, P. McKenna, D. Neely, J. Osterholz, R. Prasad, K. Quinn, B. Ramakrishna, G. Sarri, O. Willi, X. Yuan, M. Zepf, and M. Borghesi, Ion Acceleration in Multispecies Targets Driven by Intense Laser Radiation Pressure, Phys. Rev. Lett. **109**, 185006 (2012).

[14] X. Q. Yan, H. C. Wu, Z. M. Sheng, J. E. Chen, and J. Meyer-ter-Vehn, Self-Organizing GeV, Nanocoulomb, Collimated Proton Beam from Laser Foil Interaction at $7 \times 10^{21}\,\mathrm{W/cm^{-2}}$, Phys. Rev. Lett. **103**, 135001 (2009).

[15] S. Steinke, A. Henig, M. Schnürer, T. Sokollik, P. V. Nickles, D. Jung *et al.*, Efficient ion acceleration by collective laser-driven electron dynamics with ultrathin foil targets, Laser Particle Beams. **28**, 215 (2010).

[16] W. P. Wang, B. F. Shen, M. Zhang, L. L. Ji, M. Wen, J. C. Xu *et al.*, Efficient acceleration of monoenergetic proton beam by sharp front laser pulse, Phys. Plasmas. **18**, 013103 (2011).

[17] B. M. Hegelich, I. Pomerantz, L. Yin, H. C. Wu, D. Jung, B. J. Albright *et al.*, Laser-driven ion acceleration from relativistically transparent nanotargets, New J. Phys. **15**, 085015 (2013).

[18] S. Palaniyappan, C. Huang, D. C. Gautier, C. E. Hamilton, M. A. Santiago, C. Kreuzer *et al.*, Efficient quasimonoenergetic ion beams from laser-driven relativistic plasmas, Nat. Commun. **6**, 10170 (2015).

[19] W. J. Ma, I. J. Kim, J. Q. Yu, I. W. Choi, P. K. Singh, H. W. Lee, J. H. Sung, S. K. Lee, C. Lin, Q. Liao, J. G. Zhu, H. Y. Lu, B. Liu, H. Y. Wang, R. F. Xu, X. T. He, J. E. Chen, M. Zepf, J. Schreiber, X. Q. Yan, and C. H. Nam, Laser Acceleration of Highly Energetic Carbon Ions using a Double-Layer Target Composed of Slightly Underdense Plasma and Ultrathin Foil, Phys. Rev. Lett. **122**, 014803 (2019).

[20] D. Jung *et al.*, Efficient carbon ion beam generation from laser-driven volume acceleration, Phys. Plasmas **20**, 083103 (2013).

[21] E. L. Clark, K. Krushelnick, M. Zepf, F. N. Beg, M. Tatarakis, A. Machacek *et al.*, Energetic Heavy-Ion and Proton Generation from Ultra-Intense Laser-Plasma Interactions with Solids, Phys. Rev. Lett. **85**, 1654 (2000).

[22] B. M. Hegelich, B. J. Albright, J. Cobble, K. Flippo, S. Letzring, M. Paffett *et al.*, Laser acceleration of quasimonoenergetic MeV ion beams, Nature **439**, 441 (2006).

[23] J. Braenzel, A. A. Andreev, K. Platonov, M. Klingsporn, L. Ehrentraut, W. Sandner, and M. Schnurer, Coulomb-Driven Energy Boost of Heavy Ions for Laser-Plasma Acceleration, Phys. Rev. Lett. **114**, 124801 (2015).

[24] J. Li, P. Forestier-Colleoni, M. Bailly-Grandvaux, C. McGuffey, A. V. Arefiev, S. S. Bulanov *et al.*, Laser-driven acceleration of quasimonoenergetic, near-collimated titanium ions via a transparency-enhanced acceleration scheme, New J. Phys. **21**, 103005 (2018).

[25] H. Kiriyama, A. S. Pirozhkov, M. Nishiuchi, Y. Fukuda, K. Ogura, A. Sagisaka *et al.*, High-contrast high-intensity repetitive petawatt laser, Opt. Lett. **43**, 2595 (2018).

[26] A. S. Pirozhkov, Y. Fukuda, M. Nishiuchi, H. Kiriyama, A. Sagisaka, K. Ogura *et al.*, Approaching the diffraction-limited, bandwidth-limited Petawatt, Optics Express. **25**, 20486 (2017).

[27] http://www.fastlite.com/en/ar824651-823532-Wizzler.html?Cookie=set.

[28] http://www.gafchromic.com/gafchromic-film/index.asp.

[29] S. Augst, D. Strickland, D. D. Meyerhofer, S. L. Chin, and J. H. Eberly, Tunneling Ionization of Noble Gases in High-Intensity Laser Field, Phys. Rev. Lett. **63**, 2212 (1999).

[30] P. Leblanc and Y. Sentoku, Scaling of resistive guiding of laser-driven fast-electron currents in solid targets, Phys. Rev. E **89**, 023109 (2014).

[31] L. Spitzer, Jr., *Physics of Fully Ionized Gases* (Interscience, New York, 1956), Chap. 5.

[32] S. C. Wilks, W. L. Kruer, M. Tabak, and A. B. Langdon, Absorption of Ultraintense Laser Pulses, Phys. Rev. Lett. **69**, 1383 (1992).

[33] W. Lotz, Electron-impact ionization cross-sections for atoms up to Z-108, Z. Physik. **232**, 101 (1970).

[34] H. A. Kramers, On the theory of x-ray absorption and of the continuous x-ray spectrum, Philos. Mag. **46**, 836 (1923).

[35] H. Sawada, Y. Sentoku, A. Bass, B. Griffin, R. Pandit, F. Beg *et al.*, Characterization of intense laser-produced fast electrons using hard x-rays via bremsstrahlung, J. Phys. B: At. Mol. Opt. Phys. **48**, 224008 (2015).

[36] R. R. Pandit and Y. Sentoku, Higher order terms of radiative damping in extreme intense laser-matter interaction, Phys. Plasmas. **19**, 073304 (2012).

[37] P. McKenna, K. W. D. Ledingham, J. M. Yang, L. Robson, T. McCanny, S. Shimizu, R. J. Clarke, D. Neely, K. Spohr, R. Chapman, R. P. Singhal, K. Krushelnick, M. S. Wei, and P. A. Norreys, Characterization of proton and heavier ion acceleration in ultrahigh-intensity laser interactions with heated target foils, Phys. Rev. E **70**, 036405 (2004).

[38] J. C. Fernandez *et al.*, Laser-ablation treatment of short-pulse laser targets: Toward an experimental program on energetic-ion interactions with dense plasmas, Lasers Part. Beams **23**, 267 (2005).

[39] G. Hoffmeister *et al.*, Influence of fs-laser desorption on target normal sheath accelerated ions, Phys. Rev. STAB. **16**, 041304 (2013).

[40] M. Allen, P. K. Patel, A. Mackinnon, D. Price, S. Wilks, and E. Morse, Direct Experimental Evidence of Back-Surface Ion Acceleration from Laser-Irradiated Gold Foils, Phys. Rev. Lett. **93**, 265004 (2004).

[41] D. Offermann *et al.*, Observations of proton beam enhancement due to erbium hydride on gold foil targets, Phys. Plasmas. **16**, 093113 (2009).

[42] L. Yin *et al.*, Monoenergetic and GeV ion acceleration from the laser breakout afterburner using ultrathin target, Phys. Plasmas. **14**, 056706 (2007).

[43] K. Zeil, J. Metzkes, T. Kluge, M. Bussmann, T. E. Cowan, S. D. Kraft *et al.*, Robust energy enhancement of ultrashort pulse laser accelerated protons from reduced mass targets, Plasma Phys. Control. Fusion. **56**, 084004 (2014).

[44] M. Schollmeier, A. B. Sefkow, M. Geissel, A. V. Arefiev, K. A. Flippo, S. A. Gaillard *et al.*, Laser-to-hot-electron conversion limitations in relativistic laser matter interactions due to multi-picosecond dynamics, Phys. Plasmas. **22**, 043116 (2015).

[45] F. Dollar, T. Matsuoka, G. M. Petrov, A. G. R. Thomas, S. S. Bulanov, V. Chvykov *et al.*, Control of Energy Spread and Dark Current in Proton and Ion Beams Generated in High-Contrast Laser Solid Interactions, Phys. Rev. Lett. **107**, 065003 (2011).

[46] B. Dromey, S. Kar, and M. Zepf, The plasma mirror—A subpicosecond optical switch for ultrahigh power lasers, Rev. Sci. Instrum. **75**, 645 (2004).

[47] S. A. Reed, T. Matsuoka, S. Bulanov, M. Tampo, V. Chvykov, G. Kalintchenko *et al.*, Relativistic plasma shutter for ultra-intense laser pulses, Appl. Phys. Lett. **94**, 201117 (2009).

[48] Y. Wang, S. Wang, A. Rockwood, B. M. Luther, R. Hollinger, A. Curtis *et al.*, 0.85 PW laser operation at 3.3 Hz and high-contrast ultrahigh-intensity $\lambda = 400$ nm second-harmonic beamline, Opt. Lett. **42**, 3828 (2017).

[49] http://www.eli-np.ro/.

[50] A. Dubey, L. B. Reid, K. Weide, K. Antypas, M. K. Ganapathy, K. Riley *et al.*, Extensible component-based architecture for FLASH, a massively parallel, multiphysics simulation code, Parallel Computing **35**, 512 (2009).

[51] A. J. Kemp and J. Meyer-ter-Vehn, An equation of state code for hot dense matter, based on the QEOS description, Nucl. Instrum. Method. Phys. Res. A **415**, 674 (1998).

[52] R. M. More, K. H. Warren, D. A. Young, and G. B. Zimmerman, A new quotidian equation of state (QEOS) for hot dense matter, Phys. Fluids **31**, 3059 (1988).

[53] Y. Sentoku and A. J. Kemp, Numerical methods for particle simulations at extreme densities and temperatures: Weighted particles, relativistic collisions and reduced currents, J. Comput. Phys. **227**, 6846 (2008).

[54] R. Mishra, P. Leblanc, Y. Sentoku, M. S. Wei, and F. N. Beg, Collisional particle-in-cell modeling for energy transport accompanied by atomic processes in dense plasmas, Phys. Plasmas **20**, 072704 (2013).

[55] R. Royle, Y. Sentoku, R. C. Mancini, I. Paraschiv, and T. Johzaki, Kinetic modeling of x-ray laser-driven solid Al plasmas via particle-in-cell simulation, Phys. Rev. E **95**, 063203 (2017).

[56] J. Fuchs, Y. Sentoku, S. Karsch, J. Cobble, P. Audebert, A. Kemp, A. Nikroo, P. Antici, E. Brambrink, A. Blazevic, E. M. Campbell, J. C. Fernadez, J. C. Gauthier, M. Geissel, M. Hegelich, H. Pepin, H. Popescu, N. Renard-LeGalloudec, M. Roth, J. Schreiber, R. Stephens, and T. E. Cowan, Comparison of Laser Ion Acceleration from the Front and Rear Surfaces of Thin Foils, Phys. Rev. Lett. **94**, 045004 (2005).

[57] K. Nemoto, A. Maksimchuk, S. Banerjee, K. Flippo, G. Mourou, and D. Umstadter *et al.*, Laser-triggered ion acceleration and table top isotope production, Appl. Phys. Lett. **78**, 595 (2001).

[58] A. Maksimchuk, S. Gu, K. Flippo, D. Umstadter, and V. Yu. Bychenkov, Forward Ion Acceleration in Thin Films Driven by a High-Intensity Laser, Phys. Rev. Lett. **84**, 4108 (2000).

[59] A. Macchi, F. Cattani, T. V. Liseykina, and F. Cornolti, Laser Acceleration of Ion Bunches at the Front Surface of Overdense Plasmas, Phys. Rev. Lett. **94**, 165003 (2005).

[60] M. Zepf, E. L. Clark, F. N. Beg, R. J. Clarke, A. E. Dangor, A. Gopal *et al.*, Proton Acceleration from High-Intensity Laser Interactions with Thin Foil Targets, Phys. Rev. Lett. **90**, 064801 (2003).

[61] C. A. J. Palmer, N. P. Dover, I. Pogorelsky, M. Babzien, G. I. Dudnikova, M. Ispiriyan *et al.*, Monoenergetic Proton Beams Accelerated by a Radiation Pressure-Driven Shock, Phys. Rev. Lett. **106**, 014801 (2011).

[62] http://www.sciencemag.org/news/2018/01/physicists-are-planning-build-lasers-so-powerful-they-could-rip-apart-empty-space.

[63] J. B. Birks, Scintillations from organic crystals: Specific fluorescence and relative response to different radiations, Proc. Phys. Soc. Sect., A **64**, 874 (1951).

[64] https://phits.jaea.go.jp/index.html.

[65] http://web-docs.gsi.de/∼weick/atima/.

[66] A. J. Mackinnon, Y. Sentoku, P. K. Patel, D. W. Price, S. Hatchett, M. H. Key, C. Andersen, R. Snavely, and R. R. Freeman, Enhancement of proton acceleration by hot-electron recirculation in thin foils irradiated by ultra-intense laser pulses, Phys. Rev. Lett. **88**, 215006 (2002).